

---

# Heat Transfer from Localized Absorbing Defects to the Host Coating Material in HfO<sub>2</sub>/SiO<sub>2</sub> 351-nm High Reflectors

Recent atomic-force microscopy (AFM) studies of laser-induced damage morphology in HfO<sub>2</sub>/SiO<sub>2</sub> UV multilayers,<sup>1</sup> caused by 351-nm, 1-ns laser pulses, revealed submicron-sized craters as the dominant damage morphology in these films [see Fig. 70.29(a)]. The origin of such craters was attributed to nanoscale, localized absorbers in the film matrix, the smallest size of which was estimated to be <10 nm. However, at this time, both the exact physical nature of these absorbers and the mechanism of energy transfer to the host coating material in the promotion of damage remain speculative. Empirical evidence<sup>1</sup> suggests that, at some time in the damage evolution, melting occurs; furthermore, near damage threshold, even the smallest absorbing defects are able to induce such melting to extend to about 50 nm inside the coating. For incident fluences 5%–20% above this threshold, the crater-depth distribution shifts dramatically, as measured by AFM (see Fig. 70.29), while for the lower fluences the melt processes and crater formation are largely confined to the top HfO<sub>2</sub> layer [Fig. 70.29(b)]—these processes penetrate into the next-from-the-top, SiO<sub>2</sub> layer at fluences ~20% above threshold [Fig. 70.29(d)].

In this work, by carrying out heat-transfer calculations for the same HfO<sub>2</sub>/SiO<sub>2</sub> multilayer system, our goal was to answer the following questions:

- a. How high a temperature must an absorbing defect reach to support film-crater formation of the type observed experimentally by AFM?
- b. How does heat *conduction* affect the damage kinetics at these temperatures and for different defect and host characteristics?
- c. May heat conduction be considered the dominant energy-transfer mechanism, or must other mechanisms be included for the process physics to remain plausible?

In the following, the model assumptions and simulation results will be presented. From these results, one concludes that, for realistically sized defects and absorption conditions

for 351-nm laser light, a damage model commensurate with empirical, AFM evidence *must* account for energy-transfer mechanisms other than heat conduction alone.

## Methodology

Heat-transfer modeling was accomplished by using the finite-element analysis code ANSYS<sup>2</sup> in rigid-grid form. The equation of motion was treated in matrix form

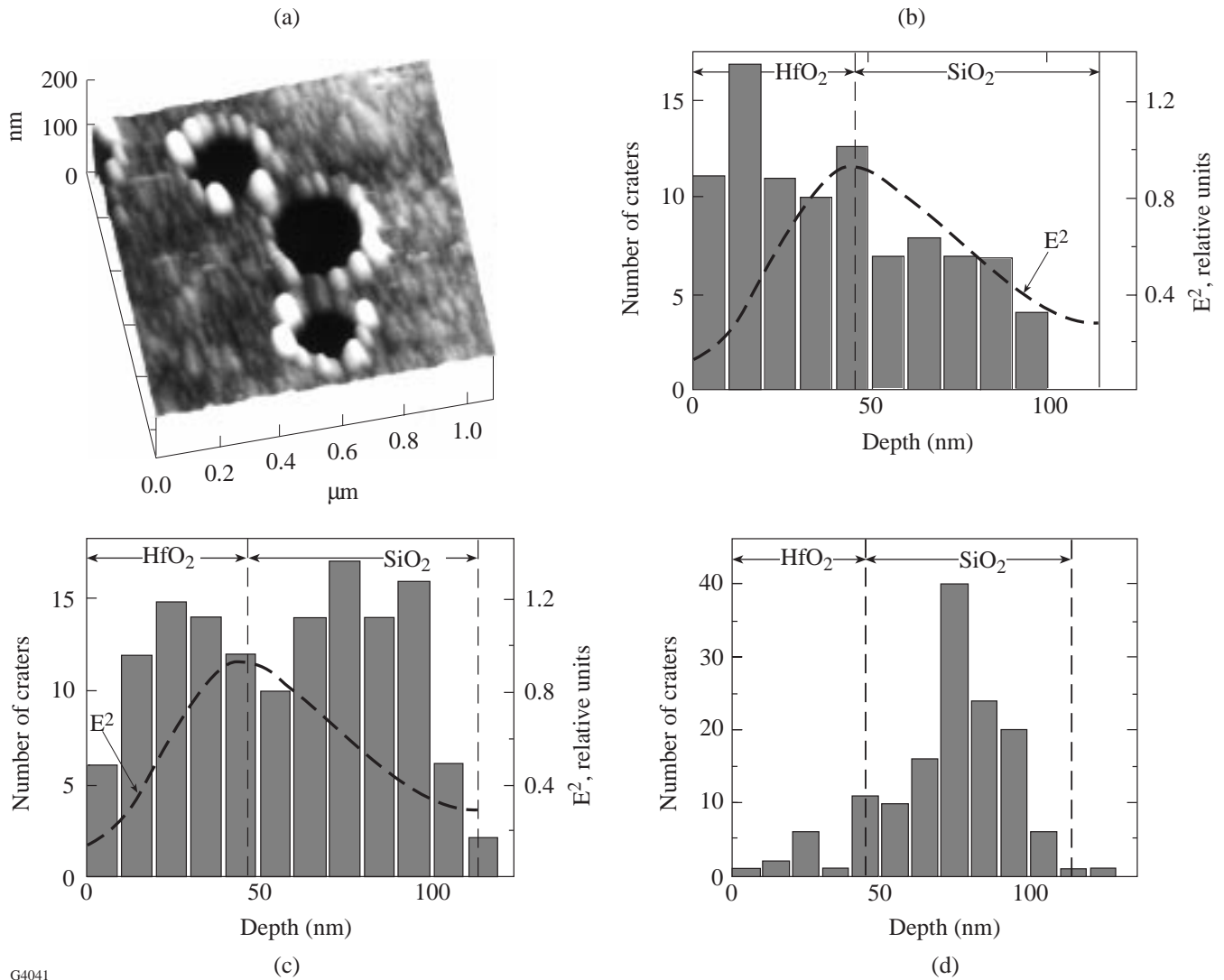
$$[c] \{\dot{T}\} + [K] \{T\} = \{Q\}, \quad (1)$$

where  $[c]$  represents the specific-heat matrix,  $[K]$  the conductivity matrix,  $\{T\}$  the nodal temperature vector, and  $\{Q\}$  the nodal heat-flow vector. The model assumed *convective* heat transfer at the film/air interface and *conduction* inside both the defect and the host material. The model geometry, depicted in Fig. 70.30, contains alternating quarter-wave layers ( $\lambda = 351$  nm) of HfO<sub>2</sub> and SiO<sub>2</sub> of cylindrical geometry with the  $r$  axis along the film/air interface, and the  $y$  axis oriented perpendicular to the layer stack. A single, cylindrical defect is placed at the thickness midpoint of the top HfO<sub>2</sub> layer, its size taking on values in accordance with data in Fig. 70.30.

Heat *generation* inside the defect is based on uniform volume absorption of the laser light at a *constant rate* throughout the 1-ns laser pulse. We assume that *non-B Beer's law* of absorption holds for these defects that are much smaller than a “skin depth.” For an absorbed fraction  $\beta$  of the light normally incident on the defect of length  $d$ , the heat-generation rate inside the defect becomes

$$H_{\text{gen}} = \beta \Phi_{\text{th}} / d \tau, \quad (2)$$

where  $\Phi_{\text{th}}$  is the damage-threshold fluence (5.6 J/cm<sup>2</sup>) and  $\tau$  is the 1-ns laser-pulse duration. As reliable absorption-coefficient data are absent for most nanoscale absorbers,  $\beta$  was fixed at a value of 0.1. For a value of  $d = 27$  nm, this yields a heat-generation rate  $H_{\text{gen}} = 2 \times 10^{20}$  J/m<sup>3</sup> s. To evaluate the relative influence of various other parameters, such as the



G4041

Figure 70.29

(a) Conventional laser-damage craters formed by 351-nm radiation in the HfO<sub>2</sub>/SiO<sub>2</sub> film. Crater-depth distributions in the HfO<sub>2</sub>/SiO<sub>2</sub> system and the electric field  $E$  of the incident light for different laser-fluence conditions: (b) ~5% above threshold fluence, (c) 10%–15% above threshold fluence, and (d) ~20% above threshold fluence.

thermal-conductivity *anisotropy* and defect size and type, this  $H_{\text{gen}}$  value was initially kept constant. Later, when agreement between empirically obtained AFM results and simulations was sought,  $H_{\text{gen}}$  values were parametrically varied.

### Material Properties

Two types of absorbing defects were considered:

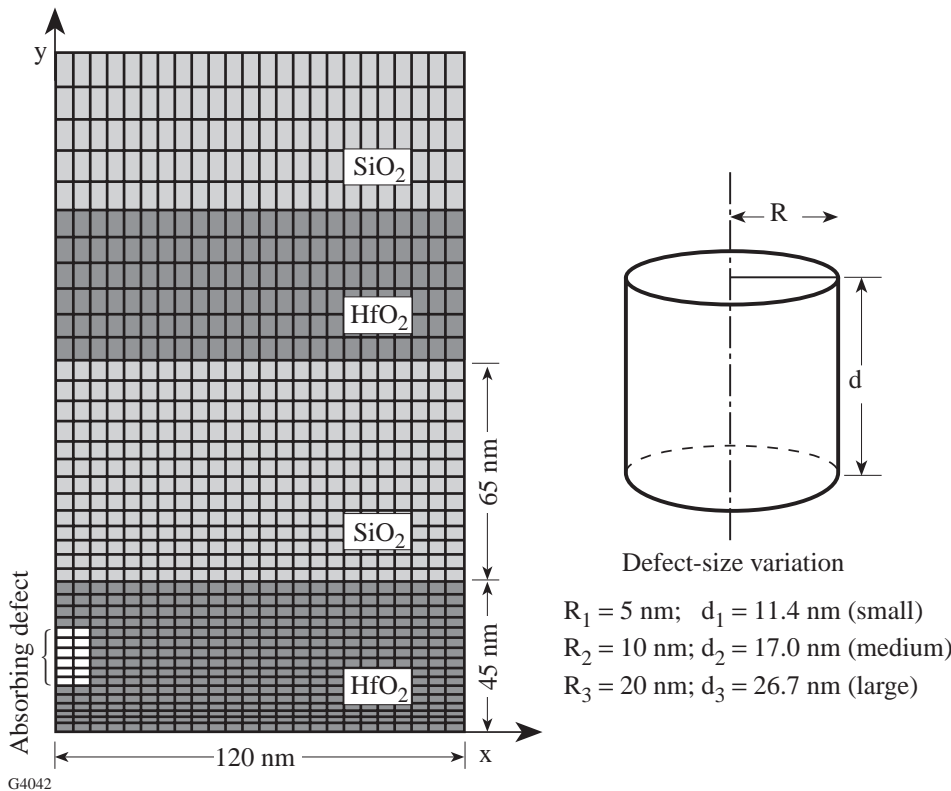
1. *Metallic Hf nanoclusters* with bulk-metal thermal parameter values for  $K$  (thermal conductivity),  $H$  (enthalpy), and  $T_m$  (melting point);

2. *Off-stoichiometric HfO<sub>2</sub> film* with the following parameters:

$K$  – HfO<sub>2</sub> *thin-film* thermal conductivity,  
 $H$  – HfO<sub>2</sub> *bulk* enthalpy, and  
 $T_m$  – HfO<sub>2</sub> *bulk* melting point.

The absorbing-defect thermal parameter values are listed in Table 70.III.

Thin-film material property values are summarized in Table 70.IV, where  $K_x$ ,  $K_y$ , and  $K_z$  are the Cartesian-



G4042

Figure 70.30 Model geometry employed for the finite-element analysis of heat transfer in the HfO<sub>2</sub>/SiO<sub>2</sub> system.

Table 70.III: Absorbing-defect thermal parameters.

Defect Type	$K$ (W/m <sup>2</sup> K)	$H$ (J/kg)	$T_m$ (°K)
Hf – metal	17.2	Hf – bulk <sup>a</sup>	2506
HfO <sub>2</sub>	0.1	HfO <sub>2</sub> – bulk <sup>a</sup>	3085

<sup>a</sup>Reference 3.

Table 70.IV: Thin-film thermal parameters.

Material	$K_y$ (W/m <sup>2</sup> K)	$K_x, K_z$ (W/m <sup>2</sup> K)	$H$ (J/kg)	$T_m$ (°K)
HfO <sub>2</sub>	0.10	0.10 $\gamma$	Bulk <sup>a</sup>	3085
SiO <sub>2</sub>	0.25	0.25 $\gamma$	Bulk <sup>a</sup>	1986

$\gamma = K_x/K_y$ ;  $K_x = K_z$ ;  $\gamma_1 = 0.1$ ;  $\gamma_2 = 0.2$ ;  $\gamma_3 = 0.5$ ;  $\gamma_4 = 1$ .

<sup>a</sup>Reference 3.

coordinate components of the thermal conductivity and  $\gamma$  is the anisotropy parameter for the thermal conductivity, i.e.,  $\gamma = 1$  for perfect isotropy. In these simulations,  $\gamma = 0.1$  was chosen for the most anisotropic case. Also, in distinguishing metallic defects from HfO<sub>2</sub>-type defects, *thin-film anisotropy* values were used for HfO<sub>2</sub>-defect properties.

Latent heat of fusion was accounted for in these calculations by enthalpy  $H$ .

**Modeling Results and Discussion**

Instantaneous temperature contours in 2-D space (Fig. 70.31) show the temperature-field evolution within the

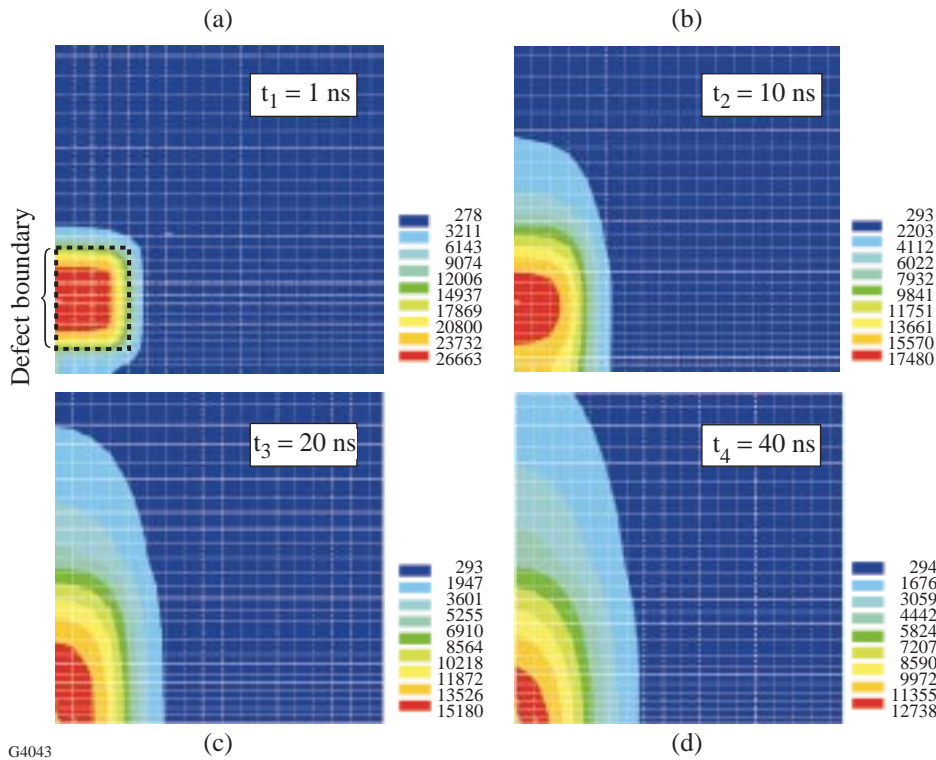


Figure 70.31

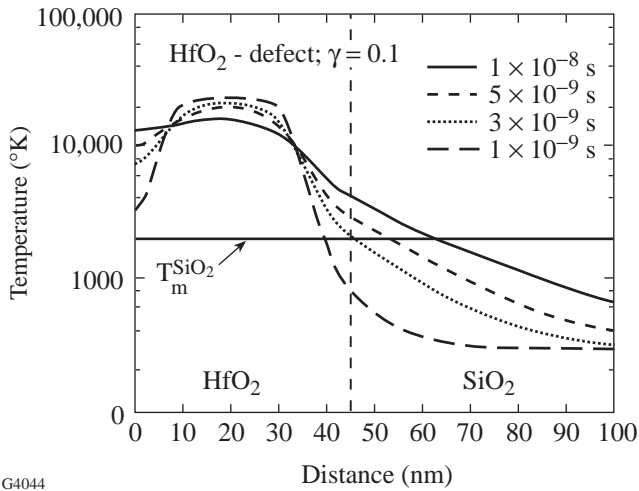
Temperature contours  $[T(^{\circ}\text{K})]$  obtained for the case of large  $\text{HfO}_2$  defect and  $\gamma = 0.1$  at various times after the beginning of the laser pulse: (a) 1 ns, (b) 10 ns, (c) 20 ns, and (d) 40 ns.

G4043

film at various times after the beginning of the laser pulse. These contours represent the case of a “large”  $\text{HfO}_2$  defect ( $R = 20$  nm;  $d = 26.7$  nm) located in the top  $\text{HfO}_2$  layer. Note that in these contours the air/film interface is located at the *bottom* of each grid and the successive film layers stack upward. One finds [Fig. 70.31(a)] that at the end of the excitation pulse the heat generated is essentially confined to the defect itself, within which the temperature reaches a value of  $2.7 \times 10^4$  °K. As time progresses, the locus of the peak temperature moves from the defect center toward the air/film interface [Fig. 70.31(b)]. As a consequence, 17 ns after the end of the pulse, the interface reaches a temperature of  $1.5 \times 10^4$  °K. On the nanosecond time scale considered in Figs. 70.31(a)–70.31(d), *convective* heat transport at this interface remains physically irrelevant and, in effect, renders this interface an adiabatic boundary, fostering the modeled temperature buildup.

Critical to the comparison with empirical crater information are the lateral temperature contours, defining the lateral scale of the melting process. One can see that in the highly anisotropic ( $\gamma = 0.1$ ) heat-conduction case represented in these figures, *lateral melt-front propagation* is fairly restricted—the melt radius remains  $<30$  nm inside  $\text{HfO}_2$ , which is nearly a factor of 2 smaller than observed during AFM mapping of craters.

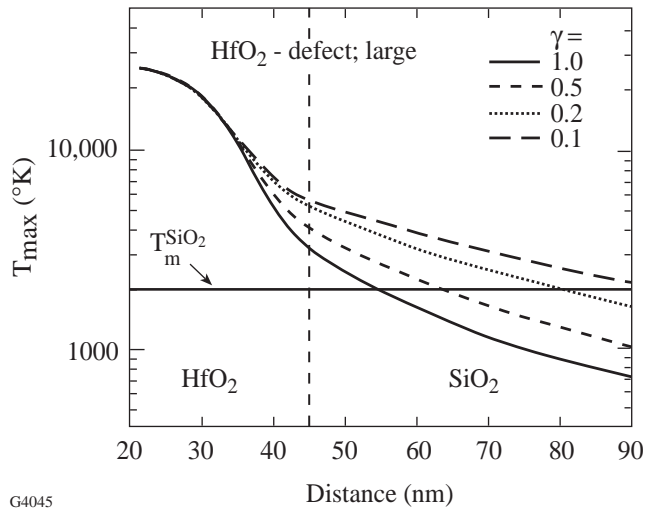
To determine the vertical-melt propagation through the film stack, Fig. 70.32 shows the *vertical* temperature around a “large”  $\text{HfO}_2$  defect as a function of depth (here the air/film interface is located at the origin) at various times after the end of the laser pulse. From Fig. 70.32 it becomes apparent that within only 3 ns after the pulse, melting starts inside the  $\text{SiO}_2$  layer (note the broken, vertical-layer-demarkation line between  $\text{HfO}_2$  and  $\text{SiO}_2$ ) and, by 10 ns after the pulse, reaches nearly halfway into the  $\text{SiO}_2$  layer. Eventually the system starts to cool down, which sets the limit on the vertical-melt propagation. Similarly, Figs. 70.33 and 70.34 show the maximum temperature reached at any instant during the process at various depths below the defect as a function of conductivity anisotropy and defect type, respectively. For all anisotropy ratios chosen (Fig. 70.33), the  $\text{SiO}_2$  layer experiences melting to some extent, up to  $\sim 75\%$  of the entire layer. The same strong dependence of melting on anisotropy also holds for the “large” Hf-metal defect (Fig. 70.34), which at the fixed, identical heating rate is completely molten and itself isotropic ( $T_m = 2506$  °K). In Figs. 70.33 and 70.34 there is a small, systematic error. The code recognizes and accounts for the change in conductivity anisotropy upon melting, but during the cool-down phase reinstates anisotropy as if the material had recovered initial crystallinity. Preliminary simulations show that this error in no way alters the seminal features or conclusions.



G4044

Figure 70.32

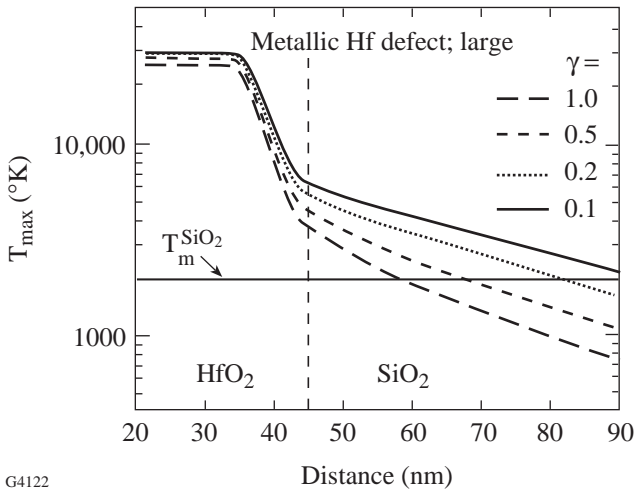
Vertical (along the  $y$  axis of the model) temperature profile kinetics (1 to 10 ns after the beginning of the laser pulse) for a “large” HfO<sub>2</sub> defect.



G4045

Figure 70.33

Maximum-temperature  $T_{\max}$  vertical profiles as a function of conductivity anisotropy  $\gamma$  for a “large” HfO<sub>2</sub> defect case.



G4122

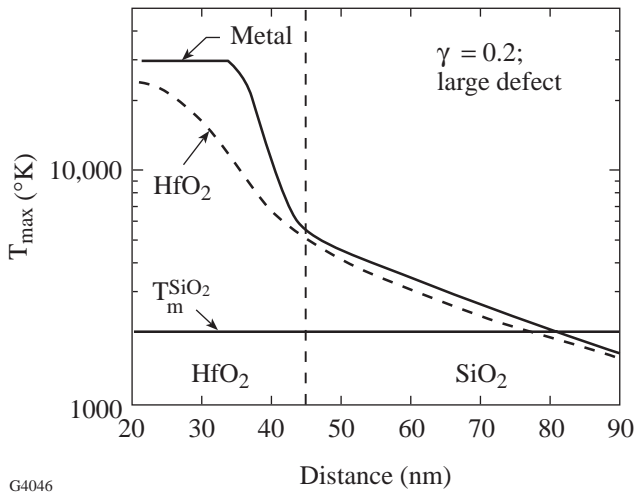
Figure 70.34

Maximum-temperature  $T_{\max}$  vertical profiles as a function of conductivity anisotropy  $\gamma$  for a “large” metallic Hf defect case.

Ignoring the differences in absorption between a metallic and an off-stoichiometric defect and simply assuming that, over the laser pulse length, *equal amounts of energy* have been deposited in either one, the relative importance of *defect* heat capacity and internal heat conductivity for energy transfer to the surrounding film is outlined in Fig. 70.35. Due to its higher conductivity, the metallic defect attains a *uniform* temperature and delivers heat rapidly to its surface. This causes the surrounding HfO<sub>2</sub> film to reach higher temperatures than if the defect consisted of off-stoichiometric HfO<sub>2</sub>. At the HfO<sub>2</sub>/

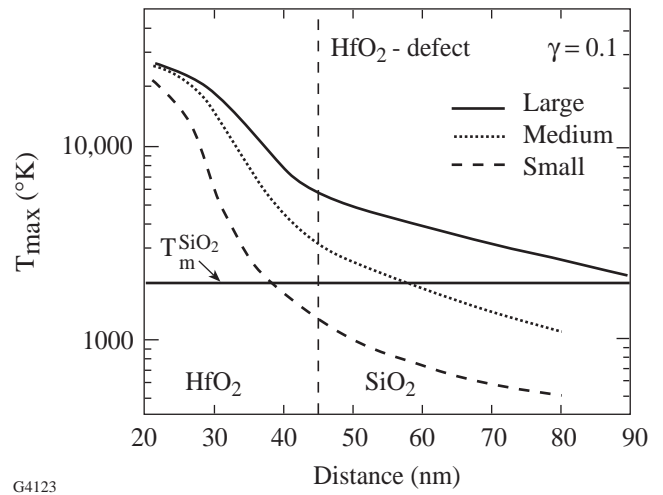
SiO<sub>2</sub> interface this difference has been mediated away by the poor conductivity of the dielectric film. The melting behavior of the SiO<sub>2</sub> layer is insensitive to the nature of the defect.

The issue now remains how, for equal energy volume density at the end of an excitation pulse, defects of various sizes (i.e., of various surface areas) affect the melting behavior of the host layer as well as that of the next-nearest neighboring layer. For the three sizes (small/medium/large) considered, the volumes scale as 1:6:37. Figures 70.36 and 70.37 plot the maximum temperatures reached inside the HfO<sub>2</sub> and SiO<sub>2</sub> layers for the three cases—Fig. 70.36 representing a dielectric defect and Fig. 70.37 a metallic defect. For the same reason as given in the discussion of Fig. 70.35 (i.e., the higher thermal conductivity of the metal), the metallic defects shed heat effectively *during* the laser pulse, providing for larger maximum-temperature differences between the defects with the various surface-to-volume ratios than for defects of dielectric composition. At threshold, neither dielectric nor metallic, *small* defects contain enough heat to melt the SiO<sub>2</sub> layer, indicating a critical defect size for melting to occur (at threshold) inside the SiO<sub>2</sub> layer. Tables 70.V and 70.VI list the melt-penetration depth  $\ell_m$  normalized, for comparison convenience with AFM measurements, to the HfO<sub>2</sub>/SiO<sub>2</sub> layer interface for both types of medium and large defects, as well as  $\ell_m$  dependence upon a range of conductivity anisotropies. The emphasis here is on weak anisotropies: for medium defects, no melt events are recorded, and even for large defects the melt penetration into SiO<sub>2</sub> is very shallow.



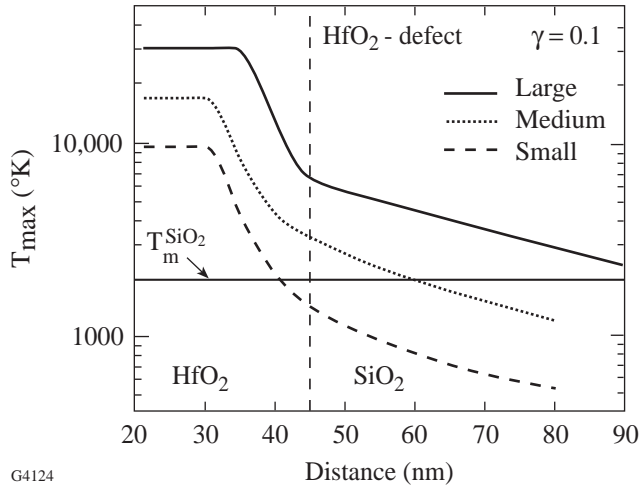
G4046

Figure 70.35  
Maximum-temperature  $T_{max}$  vertical profiles as a function of defect type. Metallic Hf versus off-stoichiometric  $HfO_2$ .



G4123

Figure 70.36  
Maximum-temperature  $T_{max}$  vertical profiles as a function of the defect size for an  $HfO_2$  defect case.



G4124

Figure 70.37  
Maximum-temperature  $T_{max}$  vertical profiles as a function of the defect size for a metallic Hf defect case.

By raising the value for  $H_{gen}$  and simulating fluence conditions *above threshold*, one may address the question of how high a temperature a given defect must reach to generate damaging melt-penetration depths comparable to experimentally observed ones. For small- and medium-sized metallic defects the corresponding melt-penetration depths  $\ell_m$  and defect peak temperatures are listed in Tables 70.VII and 70.VIII as a function of increasing  $H_{gen}$ . From these tables it becomes immediately apparent that experimentally measurable melt penetration occurs only for very high defect temperatures. For either defect size a temperature of 3 to  $4 \times 10^4$  °K is required. Such temperatures are alarming inasmuch as the physical mechanisms so far ignored in these simulations start to play a role in the overall laser-damage model. They also point toward the inability of the current model to simulate laser damage by *thermal-conductivity-dominated* energy transfer alone.

Table 70.V: Melt-penetration depth  $\ell_m$  (nm) values, large-defect case, as a function of parameter  $\gamma$ .

Defect Type	$\gamma = 0.1$	$\gamma = 0.2$	$\gamma = 0.5$	$\gamma = 1.0$
$HfO_2$	47	35	18	9
Metallic	49	38	24	14

$T_{max}(HfO_2) = 27,000$  K;  $T_{max}(met) = 30,000$  K.

Two mechanisms that spring immediately to mind have the potential for significantly altering the kinetics of laser damage by providing sources for energy absorption from the laser field *at a distance from the original defect*: thermoionically emitted electrons and blackbody radiation in both the IR and, more importantly, the UV portion of its spectrum. Still, during the excitation pulse, when the thermal energy is mostly bottled up inside the defect and its temperature is highest, free carriers directly emitted into or ionized by UV photons within the surrounding dielectric layer stack provide starting electrons for “avalanche-type” or other energy-transfer processes at locations that, in effect, constitute an electronic *ballooning* of the defect. Table 70.IX emphasizes this aspect by listing the fraction of integrated blackbody radiation with photon energy above the HfO<sub>2</sub> bandgap as a function of defect temperature, emitted by a heated defect into its surrounding. From Table 70.IX we see that 10% of the emitted blackbody spec-

trum lies above 5.6 eV for temperatures as low as  $1 \times 10^4$  °K. At the temperatures predicted by the current simulations this fraction increases to nearly 90%. The potential significance of such a UV ionization mechanism was pointed out in 1978 by Manenkov and his group.<sup>4</sup> Based on this earlier work, the Grenoble Group<sup>5</sup> evaluated the role of such preionization in single-layer films on melting and mechanical breaking of the film matrix.

Such a “larger-effective-defect” mechanism is also a plausible answer to the earlier-mentioned discrepancy between the calculated lateral-melt penetration range and the empirical AFM data. While part of this discrepancy can be assuaged by choosing a less-severe conductivity anisotropy, the lateral seeding of heating sources by ionizing radiation is an equally provocative concept whose merit must be tested in expanded simulations.

Table 70.VI: Melt-penetration depth  $\ell_m$  (nm) values, medium-defect case, as a function of parameter  $\gamma$ .

Defect Type	$\gamma = 0.1$	$\gamma = 0.2$	$\gamma = 0.5$	$\gamma = 1.0$
HfO <sub>2</sub>	13	5	0	0
Metallic	14	6	0	0

$$T_{\max}(\text{HfO}_2) = 25,000 \text{ K}; T_{\max}(\text{met}) = 17,000 \text{ K}.$$

Table 70.VII: Melt-penetration depth  $\ell_m$ , as a function of heat-generation rate  $H_{\text{gen}}$ , small-defect case.

$H_{\text{gen}}$ (W/m <sup>3</sup> )	$T_{\max}$ (°K)	$\ell_m$ (nm)
$2 \times 10^{20}$	8551	0
4	18760	1
5	22110	4
6	24750	6
7	31890	9
8	37750	12
10	42990	15

Table 70.VIII: Melt-penetration depth  $\ell_m$ , as a function of heat-generation rate  $H_{\text{gen}}$ , medium-defect case.

$H_{\text{gen}}$ (W/m <sup>3</sup> )	$T_{\text{max}}$ (°K)	$\ell_m$ (nm)
$1 \times 10^{20}$	8652	2
2	16600	14
3	27070	23
4	36970	30
5	44880	35

Table 70.IX: Fraction of thermal radiation from the absorbing defect with photon energy exceeding HfO<sub>2</sub> bandgap (5.6 eV).

$T$ (°K)	$F_{\text{ion}}$ (%)
10,000	10
20,000	57
30,000	80
40,000	89

### Summary

In considering thermal conduction as the only energy transport mechanism, the current simulations show that relevant comparison with empirical damage morphology necessitates such high defect temperatures ( $T > 30,000^\circ\text{K}$ ) that other physical mechanisms start to attain dominance. These calculations point toward a mechanism in which the thermally trapped defect (thermally trapped on a nanosecond time scale) emits ionizing radiation into the surrounding film matrix. In response to such ionization, a volume larger than the defect itself becomes absorptive to the laser field and mediates direct energy transfer to the film at locations distant from the defect.

### ACKNOWLEDGMENT

This work was supported by the U.S. Department of Energy Office of Inertial Confinement Fusion under Cooperative Agreement No. DE-FC03-92SF19460, the University of Rochester, and the New York State Research and Development Authority. The support of DOE does not constitute an endorsement by DOE of the views expressed in this article. The authors thank M. Shoup for valuable assistance in software system management.

### REFERENCES

1. S. Papernov, A. W. Schmid, J. Anzelotti, D. Smith, and Z. R. Chrzan, in *Laser-Induced Damage in Optical Materials: 1995*, edited by H. E. Bennett *et al.* (SPIE, Bellingham, WA, 1996), Vol. 2714, pp. 384–392.
2. ANSYS, Inc., P.O. Box 65, Johnson Road, Houston, PA 15342-0065.
3. I. Barin and O. Knacke, *Thermochemical Properties of Inorganic Substances* (Springer-Verlag, Berlin, 1973).
4. Yu. K. Danileiko, A. A. Manenkov, and V. S. Nechitailo, *Sov. J. Quantum Electron.* **8**, 116 (1978).
5. J. Dijon *et al.*, in *Laser-Induced Damage in Optical Materials: 1995*, edited by H. E. Bennett *et al.* (SPIE, Bellingham, WA, 1996), Vol. 2714, pp. 416–419.

